



Pergamon

Available online at www.sciencedirect.com

SCIENCE @ DIRECT®

Acta Materialia 51 (2003) 4171–4181



www.actamat-journals.com

Colossal carbon supersaturation in austenitic stainless steels carburized at low temperature

Y. Cao, F. Ernst*, G.M. Michal

Department of Materials Science and Engineering, Case Western Reserve University, 10900 Euclid Avenue, Cleveland, OH 44106-7204, USA

Received 2 October 2002; received in revised form 22 April 2003; accepted 26 April 2003

Abstract

A novel, low-temperature (470 °C) gas-phase carburization treatment, developed by the Swagelok Company, increases the surface hardness of 316 austenitic stainless steels from ≈ 200 to ≈ 1000 HV25 and improves the corrosion resistance. While normally the precipitation of carbides restricts the carbon concentration in the austenite of 316 steels to <0.015 at%, the Swagelok treatment generates a *colossal supersaturation* of up to 12 at% carbon in solid solution. Only upon extended treatment, does carbide precipitation eventually occur, but the colossal carbon supersaturation of the austenite is maintained. Unusual for austenitic stainless steels, the precipitates are Hägg carbide (M_5C_2). © 2003 Acta Materialia Inc. Published by Elsevier Science Ltd. All rights reserved.

Keywords: Austenitic steels; Surface alloying; Colossal supersaturation; Bulk diffusion; Hardness

1. Introduction

Among the micromechanisms available for alloy hardening, solid–solution hardening by interstitial solutes is particularly effective. Often, it is desirable to harden only at the surface, after the final part has been formed. For steel, such “case hardening” of the final parts can be achieved by carburization—inward diffusion of carbon from the surface.

Limitations to surface hardening of steels by carburization arise, however, from the limited solu-

bility of carbon. This is particularly true for austenitic stainless steels. Carburization of austenitic stainless steels is usually carried out at high temperatures, up to 1010 °C, enabling rapid precipitation of chromium carbides at the carburized surface [1]. While carbide precipitation does increase the surface hardness (up to 750 HV), the precipitates substantially reduce the concentration of chromium in the austenite. Therefore, carbide precipitation greatly reduces the corrosion resistance, thus obliterating one of the major advantages of austenitic stainless steels.

To circumvent this problem, the Swagelok Company has recently developed a *low-temperature* carburization technology for austenitic stainless steels. The carburization temperature of this process is between 465 and 475 °C. In order to study

* Corresponding author. Tel.: +1-216-368-0611; fax: +1-216-368-3209.

E-mail address: fxe5@po.cwru.edu (F. Ernst).

Table 1
Major elements of the studied materials (at%)

	C	Mn	Si	P	S	Cr	Ni	Mo	Fe
KMD-A	0.23	1.79	1.18	0.04	0.04	18.45	11.62	1.19	64.94
KJL-A	0.21	1.63	0.34	0.03	0.05	18.50	12.55	1.51	64.68
P42860	0.11	1.35	0.79	0.04	0.01	17.97	9.85	1.22	68.65

the microstructural changes involved in such low-temperature carburization, we have studied bulk specimens, thin foils, and powders of several different low-temperature-carburized 316 stainless steels by X-ray diffraction (XRD), X-ray photoelectron spectroscopy (XPS or “ESCA”, electron spectroscopy for chemical analysis), scanning electron microscopy (SEM), and transmission electron microscopy (TEM). In the present publication, we focus on results obtained by XRD, XPS, and SEM of bulk and powder specimens. A subsequent publication will present the results obtained by TEM [2].

2. Experimental methods

Table 1 lists the compositions of the materials we have studied (in atomic percent, prior to carburization, major elements only). As summarized in Table 2, KMD-A and KJL-A were provided as cm-sized bars, which had been carburized for 246 h at 470 °C. The “A” in the sample designation indicates that these specimens had been *annealed* for 1 h at 1065 °C prior to the carburization treatment. The specimen P42860 was a *powder* with a mean grain size of 16 µm, which had been carburized for 149 h at 465 °C. The carburization of all specimens was carried out at the Swagelok Company in a gas mixture of N₂, CO, and H₂ at atmospheric

pressure in repeated process runs, adding up to the carburization times listed in Table 2.

All specimens were examined before and after carburization by XRD with monochromated Cu-K_α radiation, generated with 45 keV electrons and a current of 40 mA, in a Scintag X-1 X-ray diffraction instrument. XRD scans were recorded in the standard θ - θ Bragg–Brentano geometry, typically in the range $20^\circ < 2\theta < 100^\circ$ with steps of 0.02° and counting times of 1.2 or 10 s/step. A computer system with DMS NT software served to control the diffractometer and to acquire and analyze raw data. In order to simulate XRD scans, we employed the Rietveld analysis software RIETAN-2000 by Izumi [3,4]. In order to acquire XRD scans at different depths below the surface of carburized bulk specimens, thin layers were successively removed from the specimen surface by grinding and polishing them with SiC grinding papers down to grit 1200.

In addition to the XRD studies, we applied XPS (ESCA) as well as SEM. SEM was used for metallographic studies of the carburized materials. We used a Hitachi S-4500, equipped with a field-emission gun, two secondary-electron detectors, and a backscatter detector. This instrument achieves a spatial resolution of less than 1.5 nm at a primary electron energy of 15 keV. SEM specimens of the carburized bulk samples KMD-A and KJL-A were prepared by cutting cross-sections, grinding and

Table 2
Carburization treatments of the studied materials

Sample	Morphology	Annealed	T _c (°C)	t _c (h)
KMD-A	Bar stock	1.0 h at 1065 °C	470	246
KJL-A	Bar stock	1.0 h at 1065 °C	470	246
P42860	Powder, $\phi \approx 16$ µm	–	465	149

polishing the cross-sectional surface with grit 600 SiC paper and 1 μm diamond paste, and etching in Marble's reagent (10 g CuSO_4 , 50 ml HCl, and 50 ml H_2O) to reveal the microstructure.

XPS was carried out in a Perkin-Elmer PHI-5600 ultra-high vacuum system with a monochromated aluminum anode X-ray source, a multi-channel detector, a 50 cm hemispherical electron energy analyzer, and an inert-gas sputtering source for sample cleaning and depth profiling. Quantitative analysis of the XPS measurements was carried out using peak-area sensitivity factors [5], based on empirical data [6] corrected for the transmission function of the spectrometer.

3. Results

3.1. Scanning electron microscopy and hardness profile

Fig. 1 presents a cross-sectional SEM image of carburized KJL-A. Directly below the surface of the specimen (vertical, on the left), the micrograph reveals a 70 μm thick layer, which was substantially less attacked by the etchant than the regular austenite further below (on the right in Fig. 1). This observation indicates that low-temperature carburization *improves* the corrosion resistance of austenitic stainless steels.

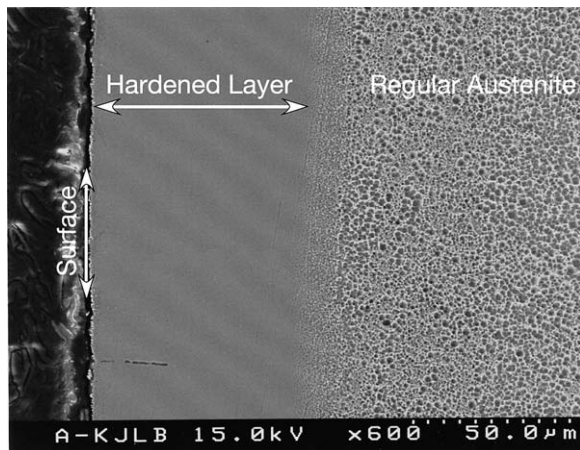


Fig. 1. Cross-sectional SEM image of a low-temperature carburized 316 austenitic stainless steel specimen (KJL-A).

Fig. 2 depicts the hardness of carburized KJL-A as a function of depth z below the surface (courtesy of Swagelok). Near the surface, the hardness is ≈ 1000 HV25. For an austenitic steel, this hardness is truly *outstanding*: 1000 HV25 is harder than any ferritic steel, and even harder than some carbides, e.g. Cr_{23}C_6 . The hardness of the uncarburized KJL-A far below the surface, in contrast, was less than 200 HV25 (“core” in Fig. 2).

3.2. Lattice parameters prior to carburization

In order to investigate how low-temperature carburization affects the lattice parameter of the treated material, we first assessed the lattice parameters of the different stainless steels before carburization. For this purpose, we have obtained XRD scans from *untreated* KMD-A and KJL-A specimens, as well as from *untreated* powder P42860. High-precision assessment of the lattice parameter requires eliminating systematic errors introduced by accidental vertical displacement of the sample surface vs. the diffractometer axis. This is achieved

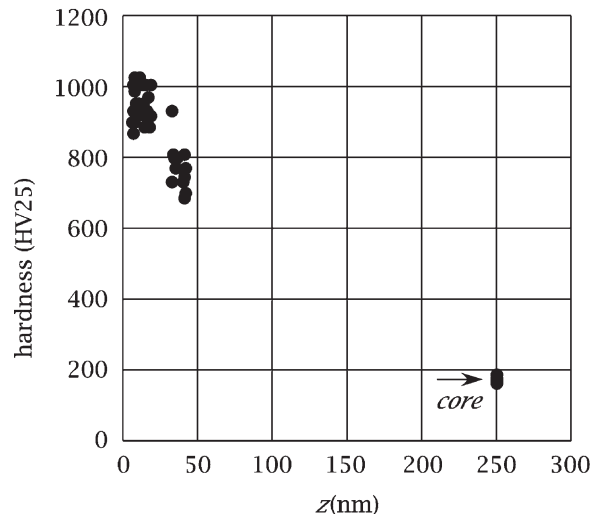


Fig. 2. Depth profile of the hardness (Vickers hardness measured with a load of 25 g) in KJL-A. The relatively large scatter of the hardness data, particularly at near the surface, originates from the necessity of indenting with a small load in order to obtain sufficient spatial resolution. Consequently, the indents are very small, and an error of only 0.5 μm in measuring the indent size will result in an error of ± 200 HV25. (Courtesy of Swagelok Company.)

by extrapolating the lattice parameters obtained from the individual peak positions to $\theta = 90^\circ$ in a plot of the lattice parameters vs. the Nelson–Riley extrapolation function $\cos[\theta]\cot[\theta]$ [7]. Fig. 3 shows the fitted data for all three materials. For comparison, the data we obtained from KMD-A after carburization are also included.

All data sets recorded before carburization yielded essentially the same lattice parameter: (0.36004 ± 0.00008) nm for KMD-A, (0.3597 ± 0.0001) nm for KJL-A, and (0.35985 ± 0.00002) nm for P42860. The linear regression line in Fig. 3 refers to the powder specimen, P42860. The regression lines of KMD-A and KJL-A are very close to this line, and the scattering of the data points around the respective regression lines is small. The data obtained from KMD-A *after carburization*, in contrast, indicate a significantly larger lattice parameter than KMD-A before carburization. Accordingly, low-temperature carburization substantially *expands* the austenite lattice. Moreover, the scattering of the data points around the regression line is much more pronounced than before carburization. This feature can be explained as a systematic shift of individual peaks with respect to each other, caused by the formation of a high density of stacking faults on $\{111\}$ planes of the austenite [8–10]. Indeed, the existence of a

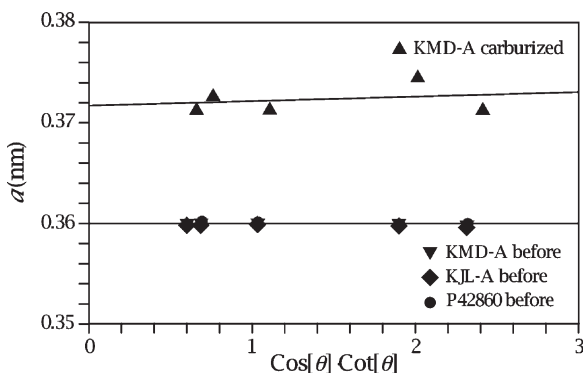


Fig. 3. High-precision assessment of the austenite lattice parameter prior to carburization (three overlapping graphs at the bottom) and in sample KMD-A after carburization (topmost graph). The true lattice parameter is obtained by extrapolating the lattice parameters obtained from the individual peak positions to $\theta = 90^\circ$ in a plot of the lattice parameter vs. $\cos[\theta]\cot[\theta]$ (Nelson–Riley correction).

high density of stacking faults in the austenite matrix near the surface is likely since TEM images indicate a high density of dislocations in this region [2], generating a high density of stacking faults by dissociating into partial dislocations because the stacking-fault energy of γ -Fe is relatively low [11].

3.3. The carburized austenite

Fig. 4 presents a series of XRD scans obtained from a carburized KMD-A specimen after successive removal of thin layers from the planar surface. Under the experimental conditions we employed, the sampling depth of the XRD scans below the specimen surface amounts to about $5 \mu\text{m}$. All scans in Fig. 4 exhibit the $\{111\}$ and $\{200\}$ peaks of austenite. In addition to these peaks, the scan recorded at the surface ($z = 0 \mu\text{m}$; z denotes the coordinate into the specimen) and at a depth of $z = 20 \mu\text{m}$ below the original surface exhibit peaks that *cannot* be ascribed to austenite. Accordingly, these peaks belong to a second phase, which has formed in the austenite within the first $30 \mu\text{m}$ below the surface during low-temperature carburization. The most intense peak of this phase occurs

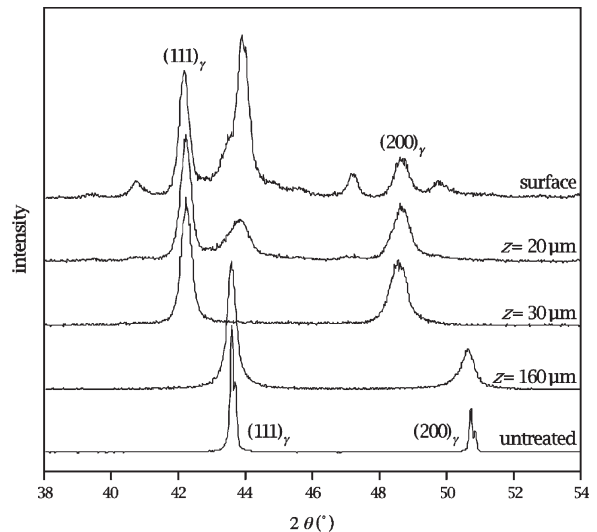


Fig. 4. XRD scans obtained from carburized 316 austenitic stainless steel KMD-A at different depths z below the surface, obtained after successive removal of layers from the planar surface. The scan at the bottom was obtained from *untreated* KMD-A.

at $2\theta = (43.87 \pm 0.20)^\circ$, which corresponds to a plane spacing $d = (0.2057 \pm 0.0010)$ nm. As shown below, the second phase has the crystal structure of Fe_5C_2 , the “Hägg” or “ χ ” carbide [12].

Equivalent results were obtained for carburized KJL-A. Fig. 5 presents the XRD scans recorded from carburized KJL-A at different depths z below the surface. Similar to Fig. 4, the line scans recorded at $z = 0, 3, \text{ and } 7 \mu\text{m}$ indicate the presence of the carbide phase. The major difference between KJL-A and KMD-A is that the carbide peaks of KJL-A are somewhat less intense relative to the austenite peaks.

For comparison, Figs. 4 and 5 also include XRD scans obtained from KMD-A and KJL-A prior to carburization (bottom). Compared to the XRD patterns obtained prior to carburization, the austenite peaks of the carburized material in Figs. 4 and 5 are uniformly shifted towards smaller diffraction angles. The peak shift, most strongly observed in the scans recorded a short distance below the carburized surface, confirms that low-temperature carburization causes a substantial expansion of the austenite lattice. Furthermore, the diffraction peaks recorded at small depths z below the surface are significantly broader than those recorded from the

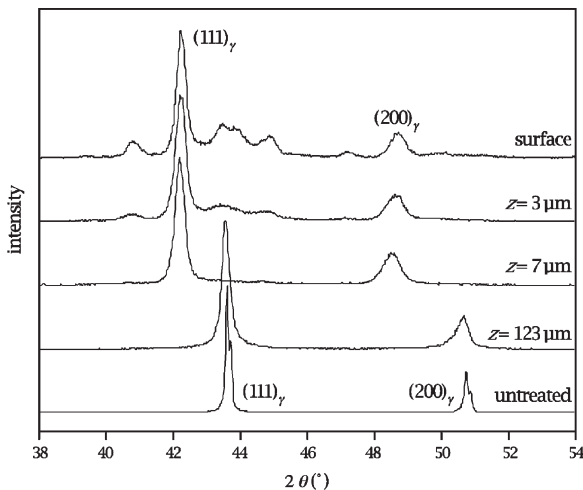


Fig. 5. XRD scans obtained from carburized 316 austenitic stainless steel KJL-A at different depths z below the surface, obtained after successive removal of layers from the planar surface. The scan at the bottom was obtained from untreated KMD-A.

untreated specimen. In fact, our TEM studies [2] revealed a very fine dispersion of carbide particles in the carburized austenite, generating austenite domains of nanoscopic dimensions that could account for such peak broadening. Stacking faults, already mentioned in conjunction with shifts of individual peaks with respect to each other, can also account for the peak broadening [8–10,13].

In the presence of interstitial solutes, an expansion of the austenite lattice is actually expected. For the particular case of carbon as the interstitial solute, the following linear relation has been empirically established between the lattice parameter a^γ and the carbon mole fraction X_C^γ in the austenite [14–17]:

$$a^\gamma = a_0^\gamma + \alpha X_C^\gamma. \quad (1)$$

In this equation, a_0^γ denotes the lattice parameter of elemental γ -Fe (without carbon), and α is an empirical parameter. Relation (1) implies that X_C^γ can be assessed from measured values for the lattice parameters a_0^γ and a^γ before and after carburization.

The carbon concentration profiles $X_C^\gamma[z]$ below the surface of the carburized specimens were obtained by determining austenite peak positions in each line scan of Figs. 4 and 5, obtaining the precise lattice parameters $a^\gamma[z]$ by the extrapolation method of Fig. 3, and computing the corresponding carbon concentration X_C^γ from (1). For a_0^γ we used the lattice parameters we obtained from XRD scans of the untreated materials. Some uncertainty persists in the literature regarding the correct value of α [15]. For the present analysis, we used $\alpha = 0.0044 \text{ nm/wt\%}$ ($=0.00104 \text{ nm/at\%}$ for $X_C^\gamma \rightarrow 0$), a value that was obtained by particularly precise measurements [16]. Fig. 6 depicts a depth profile $X_C^\gamma[z]$ for the carbon concentration into the austenite of the KMD-A sample of Fig. 4. Fig. 7 displays the corresponding results for the KJL-A sample. In both graphs, the accuracy in assessing the lattice parameter by the extrapolation method of Fig. 3 is so accurate [7] that the error bars are smaller than the diameter of the data points.

Figs. 6 and 7 indicate a carbon concentration of $\approx 12 \text{ at\%}$ at the surface ($z = 0$) of both carburized specimens, KMD-A and KJL-A. To interpret this result, consider the equilibrium solubility of carbon

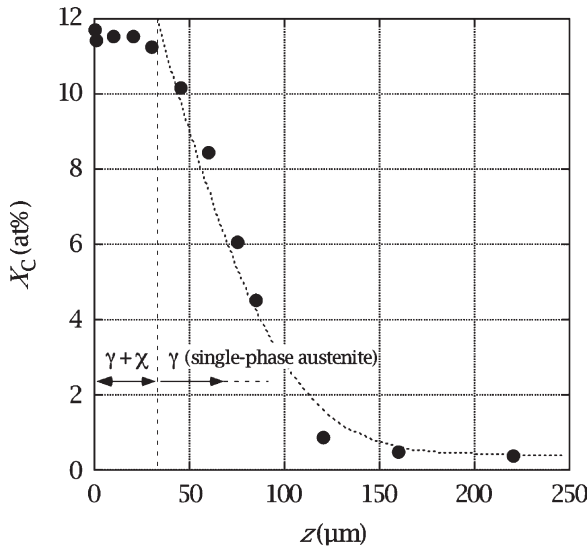


Fig. 6. Depth profile $X_C[z]$ of the carbon concentration into the *austenite* of the KMD-A sample of Fig. 4, obtained via relation (1). The dashed line represents a fit based on an error-function-type solution of Fick's second law.

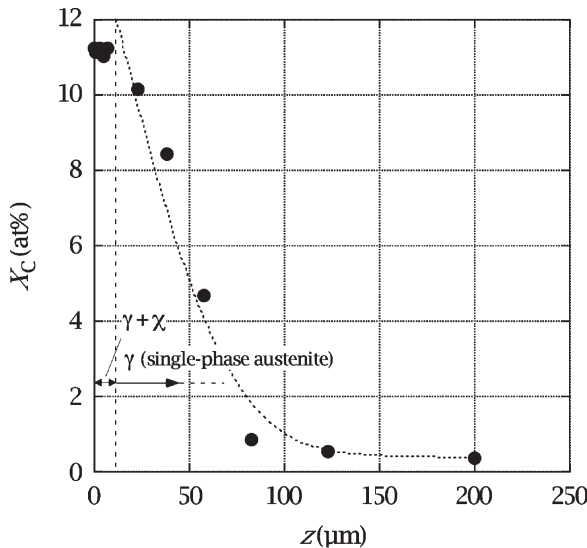


Fig. 7. Depth profile $X_C[z]$ of the carbon concentration in the *austenite* of the KJL-A sample of Fig. 5. The dashed line represents a fit based on an error-function-type solution of Fick's second law.

in 316 stainless steel at the carburization temperature. The equilibrium solubility is limited by precipitation of the carbide Cr_7C_3 , and according to a thermodynamic analysis based on published thermodynamic data [18–20], it amounts to no more than 0.015 at% carbon at 470 °C [21]. A concentration of 12 at% carbon, therefore, corresponds to ≈ 800 times the equilibrium solubility—a *colossal* carbon supersaturation of the austenite.

Near the surface, the carbon concentration profiles of both specimens exhibit a plateau, somewhat more developed for KMD-A than for KJL-A. With increasing depth z , the carbon concentration X_C then falls off in a fashion one would expect for the concentration $C_C = N_V \cdot X_C$ (N_V the number of atoms per unit volume) according to Fick's second law (with a concentration-independent diffusion coefficient D_C) for the inward diffusion of carbon from an infinite source maintaining the surface carbon concentration at C_s^C [22]:

$$C_C[z,t] = C_s^C - (C_s^C - C_0^C) \cdot \text{Erf}\left[\frac{z}{2\sqrt{D_C \cdot t}}\right], \quad (2)$$

where t denotes the time, C_s^C the carbon concentration at the surface, and C_0^C the initial carbon concentration. Fitting (2) to the data in Figs. 6 and 7 with the diffusion coefficient D_C and C_s^C as the only fitting parameters, we obtained the dashed graphs. The corresponding values for the diffusion coefficient are $1.7 \times 10^{-11} \text{ cm}^2 \text{ s}^{-1}$ for KMD-A and $1.2 \times 10^{-11} \text{ cm}^2 \text{ s}^{-1}$ for KJL-A. These values are smaller than the carbon diffusion coefficient of $D_C(470 \text{ °C}) = 6.25 \times 10^{-11} \text{ cm}^2 \text{ s}^{-1}$ one obtains by extrapolating the carbon-concentration-dependent expression that Mehl et al. [23,24] derived for D_C in Fe–C to 6 at% carbon. But a smaller value is in fact expected in (regular) 316 austenitic stainless steel because chromium decreases the diffusivity of carbon in austenite [25,26]. Agarwala et al. [25] actually measured D_C in 316 austenitic stainless steels. Based on their results, one would expect $D_C(470 \text{ °C}) = 1.9 \times 10^{-12} \text{ cm}^2 \text{ s}^{-1}$. This, of course, is nearly one order of magnitude *lower* than the values of D_C obtained in the present study. The discrepancy arises because our material contains a much higher concentration of carbon. In fact, a recent review of the influence of composition on

$D\zeta$ indicates that at the relatively low temperature of 470 °C, $D\zeta$ should substantially increase with increasing carbon concentration [27].

The depth z_h at which the carbon concentration has fallen off to half of its maximum value corresponds to about 80 μm in KMD-A and 60 μm in KJL-A. If we define z_h as “the” thickness of the (actually graded) carburized layer, the z_h obtained by XRD (Fig. 7) agrees well with the thickness of 70 μm observed in the SEM image of Fig. 1. Vice versa, the comparison between Figs. 1 and 7 indicates that a concentration of at least $\approx 3\%$ carbon is required for corrosion resistance against Marble’s etchant.

3.4. X-ray photoelectron spectroscopy

The astonishing result of a colossal carbon supersaturation in the austenite of the low-temperature-carburized 316 austenitic stainless steels was confirmed by XPS (ESCA). This method was applied to KJL-A. Before the analysis, we removed a 23 μm thick layer from the specimen surface by electropolishing. According to the XRD scans of Fig. 5, carbides only form within the first 7 μm below the surface. At a depth of $z = 23\ \mu\text{m}$, there are clearly no carbide particles, while Fig. 7 still indicates a carbon concentration of about 10 at% in the austenite. Fig. 8 presents the atomic concentrations of carbon, iron, and oxygen we have measured by XPS while sputtering the specimen surface with Ar^+ ions. The data indicate a thin, less than 10 nm thick oxygen- and carbon-rich contamination layer on the surface. After this layer had been sputtered off, however, the 1s carbon peak moved from the position typical of the binding energy of hydrocarbon to 283 eV, the binding energy of carbidic carbon (inset of Fig. 8). This confirms that carbon is in solid solution on interstitial sites of the FCC lattice of the austenite matrix. Eventually, the carbon concentration asymptotically approaches a plateau at $\approx 10\%$. This result agrees very well with the concentration profile we obtained from the XRD scans (Fig. 7).

It may be argued that XPS tends to overestimate the carbon concentration because argon ions are more effective in sputtering iron than carbon. For the following reason, however, the resulting error

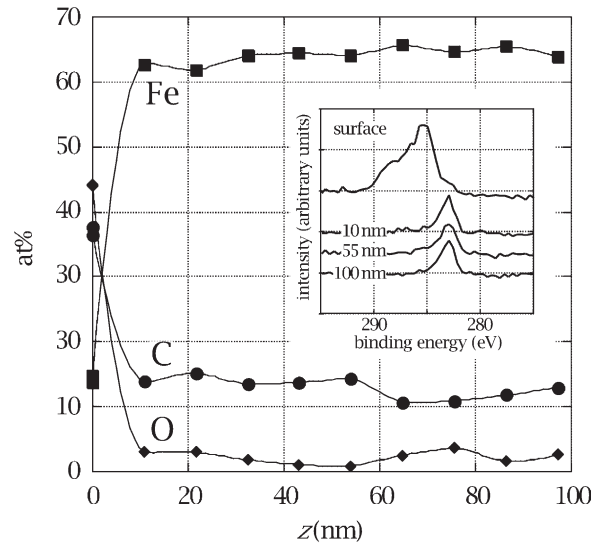


Fig. 8. Carbon, iron, and oxygen concentration in KMD-A, measured by X-ray photoelectron spectroscopy (XPS), as a function of erosion depth into the specimen. The depth follows from the time the specimen surface was sputtered with Ar ions. The inset displays how the carbon peak changes with increasing depth below the surface: the peak center moves from the position characteristic of carbohydrates to the position characteristic of carbidic carbon (283 eV). This data confirms that carbon is in solid solution on interstitial sites of the FCC lattice of the austenite matrix.

in the carbon concentration is only marginal: The 1s carbon photoelectrons used for ESCA have a kinetic energy of $\approx 1200\ \text{eV}$. Most of these electrons escape from a substantial depth of $\approx 2\ \text{nm}$ [28]. Therefore, only a small fraction of the signal in the 1s carbon peak originates from the very outer surface layer whose composition is altered by sputtering.

3.5. The carbide phase

What remains to be clarified is the nature of the phase that forms in the near-surface portion of the carburized layer, where the mean carbon concentration is even higher than the colossal solubility limit of 12 at%. XRD scans from *bulk* specimens, such as those presented in Figs. 4 and 5, are not suitable for this task because the annealing treatment the samples have undergone before carburization most likely introduced a texture, which can influence the relative peak intensities. It is for this

reason that we have studied the powder specimen P42860, carburized under exactly the same conditions as the bulk specimens.

The uppermost graph in Fig. 9 is an XRD scan obtained from the carburized powder P42860. The angular resolution of this scan is particularly high because it was acquired with 10 s of acquisition time per 2θ step of 0.02° . Contrary to Figs. 4 and 5, this scan does not exhibit any austenite peaks. The positions of the major peaks correspond to those attributed to the carbide phase in Figs. 4 and 5. Accordingly, the powder particles have been fully converted to the phase observed near the surface of the carburized bulk specimens.

In order to identify the phase in question, the XRD patterns of a variety of carbides were simulated with the RIETAN-2000 software and compared with the experimental data in Fig. 9. Ruhl and Cohen [15,29] discovered a carbon-rich phase with a hexagonal close-packed structure in rapidly

quenched Fe–C alloys, which is believed to constitute a solid solution of carbon in hexagonal iron (perhaps with short range order of the carbon positions). Owing to its simple structure, however, this ϵ -phase (not to be confused with ϵ -carbide, Fe_2C) cannot account for the additional peaks in Figs. 4 and 5. Moreover, the published electron diffraction patterns [30], as well as the instability and two-stage decomposition of the ϵ -phase at temperatures above 140 and 460 $^\circ\text{C}$, respectively, are inconsistent with our observations [2]. Therefore, we have ruled out the possibility of identifying the second phase with the ϵ -phase of Ruhl and Cohen and limited our simulations of XRD patterns to those of carbides.

A variety of carbides are known to form in steels: M_{23}C_6 , M_2C , M_3C , M_7C_3 , and M_5C_2 , where M denotes one or several metals. Simulated diffraction patterns of corresponding pure iron- and chromium carbides are shown below the experimental data in Fig. 9. Among these, only the Hägg carbide, Fe_5C_2 , yields an excellent match with the experimental XRD pattern. It can be seen that a one-to-one correspondence exists between the peaks of the simulated and the experimental graph. After refinement, the peak positions of the Hägg carbide perfectly match the experimental peak positions. Moreover, the simulated graph correctly reproduces the relative peak intensities of the experimental graph. The strongest peak of the experimental XRD scan, located at $2\theta = (44.25 \pm 0.15)^\circ$, and corresponding to a plane spacing $d = (0.2045 \pm 0.0008)$ nm, is identified as the (510) peak of the Hägg carbide.

The simulations of the other phases, in contrast, exhibit significant discrepancies with the experimental scan. From these observations, we conclude that the second phase forming in the austenite of 316 steels during low-temperature carburization is *isostructural* to the Hägg carbide, Fe_5C_2 . Since 316 steels also contain major amounts of Cr and Ni, one needs to allow for the presence of these elements in the carbide phase, too. Indeed, high-resolution *analytical* TEM has confirmed this hypothesis [31].

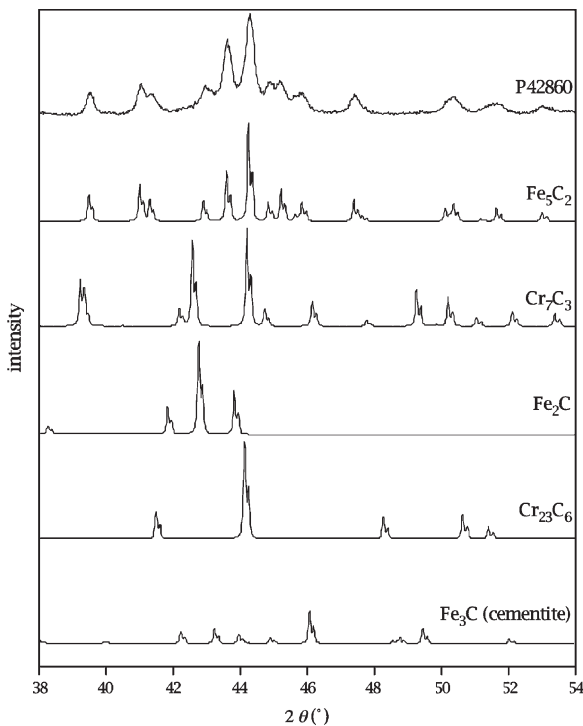


Fig. 9. XRD “slow” scan obtained from a 316 austenitic stainless steel powder after low-temperature carburization (topmost graph), and simulated XRD scans of various carbides, obtained with the RIETAN-2000 software package [3,4].

4. Discussion

The experimental results revealed that low-temperature carburization of 316 austenitic stainless steel leads to a *colossal* supersaturation of the austenite with interstitial carbon. The concentration of 12 at% carbon measured near the surface corresponds to about 800 times the equilibrium solubility of 0.015 at% at the carburization temperature. The equilibrium solubility is established by the precipitation of carbides (Cr_7C_3). The most important feature of the Swagelok process, therefore, is to suppress the formation of carbides until the carbon concentration has reached a much higher value of ≈ 12 at%. Even without a detailed thermodynamic–kinetic analysis, it is clear that one important parameter for obtaining this kind of behavior is the temperature. Carbon diffuses interstitially, while the precipitation of a carbide requires substitutional diffusion. The optimum carburization temperature identified by the Swagelok Company is low enough to prevent substitutional diffusion, but still high enough to enable sufficiently rapid interstitial transport of carbon.

The carbon concentration profiles $X_C^i(z)$ in Figs. 6 and 7 do not resemble the diffusion profile one would expect for a single phase after inward diffusion of carbon from the surface. In both diagrams, the near-surface region of the concentration profile is truncated to a plateau. The widths of these plateaus agree well with the thickness of the layer below the surface in which the carbide phase is observed in Figs. 4 and 5 and in cross-sectional TEM images [2] of KMD-A and KJL-A samples. These findings suggest that a carbon concentration of about 12 at% constitutes the solubility limit for these steels under the non-equilibrium conditions of the Swagelok process.

Exceeding the non-equilibrium solubility of ≈ 12 at% eventually causes the precipitation of Hägg carbide with the composition M_5C_2 and the crystal structure of Fe_5C_2 . The relative amounts of the different metal atoms in the carbide are anticipated to be the same as in 316 austenitic stainless steel. The crystal structure of Hägg carbide is monoclinic and is closely related to that of Fe_3C (cementite or cohenite [32]). Hägg carbide is clearly a metastable phase in all materials under consideration here. To

our knowledge, the formation of this carbide in austenitic stainless steels is very unusual and has not been reported in the literature before. Low-temperature *plasma*-carburization of austenitic stainless steels, for example, has been reported to cause the formation of Cr_7C_3 , not M_5C_2 [17,33].

Since the surface hardness, the fatigue behavior, as well as the wear- and corrosion resistance of the material treated by the Swagelok process will be influenced by the presence of carbides, it is important to understand what in particular causes the formation of Hägg carbide. The fact that Hägg carbide forms instead of e.g. Cr_7C_3 means that at 470 °C its formation must have a kinetic advantage.

The metastable Fe_5C_2 , Fe_3C , and Fe_2C carbides are only able to form when both iron and carbon are present nearly at unit (or higher) chemical activity. At the beginning of the low-temperature carburization process, however, the activity of carbon in the austenite is much less than unity. This is because chromium greatly reduces the activity coefficient of carbon in austenite [34,35]. At 470 °C, the activity of carbon in 316 austenitic stainless steel does not approach unity until the concentration of carbon in the austenite reaches ≈ 12 at%. Only when the carbon concentration reaches this very high level, will there be a thermodynamic driving force for the formation of metastable carbides.

The particular micromechanism that leads to the formation of Hägg carbide during the time-extended Swagelok process is not clear. Some insight, however, can be obtained from the literature on this carbide. Hägg carbide can be synthesized by reacting iron oxide (Fe_2O_3) with carbon monoxide at temperatures around 400 °C [12,36,37]. This observation is interesting in the present context because the time-extended Swagelok process of low-temperature carburization involves iron oxide on the specimen surface as well as CO in the carburizing gas. The formation of Hägg carbide also seems to be favored by plastic deformation [38–40]. Considering the colossal supersaturation of the austenite matrix with carbon, the carburized material must be under enormous compressive stress, and it seems conceivable that

these stresses cause considerable plastic deformation within the carburized layer.

The alloy composition of the 316 steels we studied plays an important role for the micromechanisms of carbide formation in general, and in particular for the kinetic advantage of the carbide phase M_5C_2 . It is known that Mn stabilizes M_5C_2 vs. M_3C [41], and it may be speculated that other alloying elements have similar effects, particularly Ni and Cr. For example, the slight difference in the intensity of the carbide peaks in the XRD scans of KMD-A and KJL-A suggests that Ni, which is present with substantially larger concentration in KJL-A, tends to suppress carbide precipitation. In order to influence the microstructure that results from low-temperature carburization, the effect of different alloying elements deserves further investigation.

While colossal supersaturation of the austenite matrix with carbon leads to truly outstanding properties, the precipitation of carbides is generally disadvantageous. While carbides are known to increase the flow stress of austenitic stainless steels, such precipitation hardening contributes only marginally to the surface hardness of low-temperature-carburized 316 austenitic stainless steels. This can be verified by comparing the hardness profile of Fig. 2 with the concentration-depth profile of Fig. 7 and the XRD scans of Fig. 5: at a depth of $z = 23 \mu\text{m}$, where the carbon concentration has fallen off to $X_C \approx 10 \text{ at\%}$, the carburized layer is free of carbide. Nevertheless, the hardness is still around 900 HV25. On the other hand, the carbide particles have different mechanical and electrochemical properties than the austenite matrix. Therefore their presence may compromise the fatigue and corrosion behavior of the material.

5. Conclusions

Our results demonstrate that it is possible to generate structural materials in non-equilibrium states with unusual and desirable properties by introducing colossal supersaturations through the inward diffusion of an interstitial solute under conditions that kinetically inhibit decomposition. Carburization of 316 stainless steels at low temperature can

dissolve up to 12 at% carbon in the austenite. This is possible because carbide formation is kinetically suppressed. Only if the carbon concentration exceeds the non-equilibrium solubility limit of 12 at%, precipitates of an unusual metastable carbide, “Hägg” or “ χ ” carbide (M_5C_2), form in the austenite matrix. Low-temperature colossal supersaturation of the austenite with carbon results in an outstanding surface hardness ($\approx 1000 \text{ HV25}$) and improved corrosion resistance. At the carburization temperature of $470 \text{ }^\circ\text{C}$, the effective diffusion coefficient carbon in the austenite ($1.5 \times 10^{-11} \text{ cm}^2\text{s}^{-1}$) agrees well with literature data and reflects the decreasing effect of chromium and the increasing effect carbon on the diffusivity of carbon.

Acknowledgements

We thank Peter Williams, Sunniva Collins, and Steven Marx for numerous fruitful discussions, Arthur Heuer for comments on the manuscript, and the Swagelok Company for financial support.

References

- [1] Wood WG. Handbook of stainless steels. In: Peckner D, Bernstein IM, editors. New York: Mc Graw Hill; 1977.
- [2] Ernst F, Cao Y, Michal G. 2003. [in preparation].
- [3] <http://homepage.mac.com/fujioizumi/rietan/angle—dispersive/angle—dispersive.html>
- [4] Izumi F, Ikeda T. Materials Science Forum 2000;198:321–4.
- [5] Kibel MH. Surface analysis methods in materials science. In: O'Connor DJ, Sexton BA, Smart RStC, editors. Berlin: Springer-Verlag; 1992. p. xxi.
- [6] Wagner CD, Six HA, Jansen WT, Taylor JA. Applications of Surface Science 1981;9:203.
- [7] King HW, Payzant EA. Canandan Metallurgical Quarterly 2001;40:385.
- [8] Warren BE, Warekoi EP. Journal of Applied Physics 1953;24:951.
- [9] Wagner CNJ, Tetelman AS, Otte HM. Journal of Applied Physics 1962;33:3080.
- [10] Wagner CNJ, Boisseau JP, Aqua EN. Transactions of the Metallurgical Society of AIME 1965;233:1280.
- [11] Fujita H, Ueda S. Acta Metallurgica 1972;20:759.
- [12] Hägg G. Zeitschrift für Kristallographie 1939;89:92.
- [13] Paterson MS. Journal of Applied Physics 1952;23:805.
- [14] Roberts CS. Transactions of the Metallurgical Society of AIME 1953;197:263.

- [15] Ruhl RC, Cohen M. Transactions of the Metallurgical Society of AIME 1969;245:241.
- [16] Ridley N, Stuart H. Metal Science Journal 1970;4:219.
- [17] Sun Y, Li X, Bell T. Materials Science and Technology 1999;15:1171.
- [18] Natesan K, Kassner TF. Journal of Nuclear Materials 1970;37:223.
- [19] Andersson JO. Metallurgical Transactions 1988;A 19:627.
- [20] Dinsdale AT. CALPHAD 1991;15:317.
- [21] Michal G, Cao Y, Blush J, Ernst F 2003 [in preparation].
- [22] Jost W. Diffusion in solids, 3rd ed. New York: Academic Press, 1960.
- [23] Batz W, Mehl RF, Wells C. Transactions of the Metallurgical Society of AIME 1950;188:553.
- [24] Wells C, Mehl RF. Transactions of the Metallurgical Society of AIME 1940;140:279.
- [25] Agarwala RP, Naik MC, Anand MS, Paul AR. Journal of Nuclear Materials 1970;36:41.
- [26] Farkas D, Delgado J. Scripta Metallurgica 1983;17:261.
- [27] Liu WJ, Brimacombe JK, Hawbolt EB. Acta Metallurgica et Materialia 1991;39:2373.
- [28] Tanuma S, Powell CJ, Penn DR. Surface and Interface Analysis 1988;11:577.
- [29] Ruhl RC, Cohen M. Acta Metallurgica 1967;15:159.
- [30] Dubois JM, Caer GL. Acta Metallurgica 1976;25:609.
- [31] Ernst F, Cao Y, Oba F, Michal G. 2003. [in preparation].
- [32] Jack KH, Wild S. Nature 1966;212:248.
- [33] Sun Y, Luo N, Bell T. Surface Engineering 1994;10:279.
- [34] Natesan K, Kassner TF. Metallurgical Transactions A (Physical Metallurgy and Materials Science) 1973;4:2557.
- [35] Wada F, Wada H, Elliott JF, Chipman J. Metals Transactions 1972;3:2865.
- [36] Hirano S-I, Tajima S. Journal of Materials Science 1990;25:4457.
- [37] Tajima S, Hirano S. Journal of the Japan Society of Powder and Powder Metallurgy 1991;38:153.
- [38] Deich IS, Apaev BA. Fizika Metallov i Metallovedenie 1970;29:829.
- [39] Erofeev VM, Deich IS, Apaev BA. Fizika Metallov i Metallovedenie 1977;44:116.
- [40] Koniger A, Hammerl C, Zeitler M, Rauschenbach B. Physical Review B (Condensed Matter) 1997;55:8143.
- [41] Kor GJW. Metallurgical Transactions B (Process Metallurgy) 1979;10:397.